Synthesis, Characterization, and Electrochemical Properties of $Ag_2V_4O_{11}$ and $AgVO_3$ 1-D Nano/Microstructures

Shaoyan Zhang, Weiyang Li, Chunsheng Li, and Jun Chen*

Institute of New Energy Material Chemistry, Nankai University, Tianjin 300071, P.R. China

Received: August 24, 2006; In Final Form: September 29, 2006

We report on the synthesis, characterization, and electrochemical properties of $Ag_2V_4O_{11}$ nanowires, α-$AgVO_3$ microrods, and β-$AgVO_3$ nanowires that were synthesized through a simple and facile low-temperature hydrothermal approach without any template or catalyst. It was found that by simply controlling the hydrothermal reaction parameters such as pH and dwell time, the transformation of α-$AgVO_3$ microrods to β-$AgVO_3$ nanowires were readily achieved through a "ripening−splitting model" mechanism. Electrochemical measurements revealed that the as-prepared $Ag_2V_4O_{11}$ nanowires, α-$AgVO_3$ microrods, and β-$AgVO_3$ nanowires exhibited high discharge capacities and excellent high-rate dischargeability. In particular, the β-$AgVO_3$ nanowires have much higher capacity above 3 V than that of α-$AgVO_3$ microrods, $Ag_2V_4O_{11}$ nanowires, and commercial $Ag_2V_4O_{11}$ bulk. The mechanisms for electrochemical lithium intercalation of the $AgVO_3$ nanostructures were also discussed. It is anticipated that the novel $Ag_2V_4O_{11}$ and $AgVO_3$ one-dimensional nano/microstructures are promising cathode candidates in the application of primary lithium ion batteries for implantable cardioverter defibrillators (ICDs).

Introduction

Chemical control of the structure and morphology of inorganic materials on the nanometer scale is currently attracting extensive interest.[1] Research into the area of wet chemistry is increasingly addressing the use of hydrothermal techniques to obtain more sophisticated nanostructures and thereby improved functions.[2,3] One aim for functionalized nanomaterials is to realize energy storage and conversion with high efficiency that can be achieved by batteries.[4] Lithium ion primary and rechargeable batteries represent one of the most important developments in energy storage and conversion in the past century.[5] As known, implantable cardioverter defibrillators (ICDs), which continuously monitor the heartbeat and deliver one or more high-energy electrical shocks to the heart when dangerous arrhythmias are detected, are widely applied nowadays to effectively protect hundreds of millions of cardiovascular patients against sudden cardiac death. Lithium/silver and vanadium oxide (Li/SVO) primary (non-rechargeable) batteries, which provide high power, high-energy density, and long-term stability, are state-of-the-art power sources for advanced biomedical devices and are the only type of battery for ICDs today.[6] The Li/SVO battery system is capable of supplying a continuous low-current drain on the order of microamperes to power monitoring circuits that last for 5 to 10 years, as well as rapidly providing high-current pulses at ampere level on demand to charge capacitors which supply the energy to defibrillate the heart.[7] Since Li/SVO batteries are usually cathode-limited, it is of great scientific and technological significance to improve the properties of the cathode materials, the silver and vanadium oxides (SVOs), so as to enhance the performance of such batteries.

Among the numerous SVOs that contain Ag, V, and O in a number of stoichiometric and nonstoichiometric ratios, $Ag_2V_4O_{11}$ is commercially used as a cathode material in Li/SVO batteries for ICDs because of its high specific capacity (315 mA h g^{-1}) and high-rate capability.[8] Traditionally, the synthesis of $Ag_2V_4O_{11}$ involves two kinds of methods, and both are associated with the solid-state thermal reaction.[9] One is through a decomposition reaction between the silver-containing salts (such as $AgNO_3$, Ag_2CO_3, etc.) and vanadium pentoxide (eq 1); the other is via a combination reaction between silver oxide and vanadium pentoxide (eq 2).

$$2AgNO_3/Ag_2CO_3 + 2V_2O_5 \rightarrow Ag_2V_4O_{11} + \text{nitrogen oxides/carbon oxides} \quad (1)$$

$$Ag_2O + 2V_2O_5 \rightarrow Ag_2V_4O_{11} \quad (2)$$

The above two methods both require high reaction temperature (380−500 °C), and furthermore the morphologies of the resulting products are usually irregular particles or rodlike microstructures. Recently, $Ag_2V_4O_{11}$ nanobelts[10] and nanorings[11] were indeed synthesized by a hydrothermal process. However, to the best of our knowledge, there is no report on the electrochemical study of nanostructured $Ag_2V_4O_{11}$. Meanwhile, Poeppelmeier and co-workers[12] synthesized single-crystal $Ag_4V_2O_6F_2$ by a low-temperature hydrothermal technique (around 150 °C) for 24 h (with an additional 24-h for the cooling) and found that this material has higher capacity above 3 V than the commercial $Ag_2V_4O_{11}$, which indicates that the Ag:V molar ratios of silver vanadates (such as $Ag_2V_4O_{11}$ and $AgVO_3$) have a great effect on the electrochemical properties of the Li/SVO battery. It is thus reasoned that 1-D $AgVO_3$ nanomaterials might be a potential cathode candidate for Li/SVO battery. Until now, only a few studies have focused on the fabrication of β-$AgVO_3$ nanowires,[13] nanorods,[14] nanoneedles,[15] and nanobelts.[16] However, no attempt has been reported so far regarding the fabrication of α-$AgVO_3$ nano/microstructures and the electrochemical investigation of various $AgVO_3$ nanostructures.

* Corresponding author. E-mail: chenabc@nankai.edu.cn.

10.1021/jp065478p CCC: $33.50 © 2006 American Chemical Society
Published on Web 11/18/2006

Herein, we report on the synthesis of $Ag_2V_4O_{11}$ nanowires, α-$AgVO_3$ microrods, and β-$AgVO_3$ nanowires via a simple and facile low-temperature hydrothermal approach. The transformation of different structures and morphologies of $AgVO_3$ were readily achieved by simply controlling the hydrothermal reaction parameters. Furthermore, the electrochemical properties of the as-synthesized $Ag_2V_4O_{11}$ nanowires and various one-dimensional (1-D) nano/ microstructured $AgVO_3$ were systematically investigated by cyclic voltammetry and galvanostatic charge−discharge method. The results showed that the as-prepared $Ag_2V_4O_{11}$ nanowires, α-$AgVO_3$ microrods, and β-$AgVO_3$ nanowires exhibited high discharge capacities and excellent high-rate dischargeability, and are thus promising cathode candidates in the field of primary Li/SVO batteries for ICDs.

Experimental Section

Synthesis. Silver oxide (Ag_2O), vanadium pentoxide (V_2O_5), silver nitrate ($AgNO_3$), and ammonium metavanadate (NH_4VO_3) were all of analytical grade and used as is. $Ag_2V_4O_{11}$ and β-$AgVO_3$ bulks were prepared via solid-state reaction, in which the starting materials, Ag_2O (99.0%) and V_2O_5 (99.0%), were mixed in a stoichiometric ratio and then calcined at 380 °C for 4 h in air using porcelain crucibles.

$Ag_2V_4O_{11}$ Nanowires. Amounts of 0.046 g of V_2O_5 and 0.029 g of Ag_2O were dispensed into 16 mL of deionized water, and the mixture was transferred into a 25 mL Teflon-lined stainless steel autoclave and heated at 180 °C for 24 h. The final products were collected by centrifugation, washed with deionized water and ethanol, and then vacuum-dried at 60 °C for 8 h.

α-$AgVO_3$ Microrods. An amount of 0.1359 g of $AgNO_3$ (0.8 mmol) was dissolved into 8 mL of deionized water, and equal molar NH_4VO_3 was dissolved into another 8 mL of deionized water at 80 °C. After that, the NH_4VO_3 solution was added slowly to the $AgNO_3$ solution under stirring. An orange precipitate formed immediately. After the mixture had been stirred for about 10 min, the resulting precursor suspension was transferred into a 25 mL Teflon-lined stainless steel autoclave. The autoclave was sealed and heated at 180 °C for 4 h. After the reaction, the autoclave was cooled to ambient temperature naturally. The final products were collected by centrifugation, washed with deionized water and ethanol, and then vacuum-dried at 60 °C for 4 h.

β-$AgVO_3$ Nanowires. All steps were the same as in the synthesis of α-$AgVO_3$ microrods, except the hydrothermal reaction time was extended to 12 h.

Characterization. The phase structure and morphology of the products were investigated using X-ray diffraction (XRD), scanning electron microscopy (SEM), and transmission electron microscopy (TEM). XRD patterns of the as-prepared samples were recorded by a Rigaku INT-2000 X-ray diffractometer with Cu Kα radiation. The XRD profiles were refined by the Rietveld refinement program RIETAN-2000. SEM images were taken with a JEOL JSM-6700F field emission scanning electron microscope at an accelerating voltage of 10 kV. TEM and high-resolution transmission electron microscopy (HRTEM) images were characterized by a Philips Tecnai-F20 transmission electron microscope with an accelerating voltage of 200 kV.[17] The oxidation state was analyzed with X-ray photoelectron spectroscopy (XPS) in a Kratos Axis Ultra DLD electron spectrometer.

Electrochemical Measurements. Electrochemical measurements were carried out using two-electrode cells with lithium metal as the counter and reference electrode. The working electrode was fabricated by compressing a mixture of the active materials ($Ag_2V_4O_{11}$, α-$AgVO_3$, or β-$AgVO_3$), conductive material (acetylene black-ATB), and binder (ploytetrafluoroethylene-PTFE) in a weight ratio of active material:ATB:PTFE = 8:1:1. The electrode was dried at 80 °C for 1 h and cut into a disk (1.0 cm^2). The electrolyte solution was 0.5 M $LiClO_4$ dissolved in a mixture of propylene carbonate (PC) and diethyl carbonate (DEC) with the volume ratio of PC:DEC = 1:1. The cell assembly was performed in a glove box filled with pure argon (99.999%) in the presence of an oxygen scavenger and a sodium-drying agent.

The electrochemical properties were investigated by using a PARSTAT 2273 Advanced Electrochemical System and an Arbin charge−discharge unit at controlled temperatures. The cyclic voltammograms (CV) were measured at the scan rate of 1 mV s^{-1} and 37 °C. The impedance measurements were carried out under the open-circuit condition in the frequency range from 1×10^6 to 0.1 Hz. ZSimpWin software was used for equivalent circuit fitting of the impedance data. The electrode capacity was measured by a galvanostatic discharge-charge method at a constant current of 0.01 mA or 0.1 mA to the cutoff voltage of 1.5 V and at a temperature of 37 °C. The capacity was based on the amount of the active material, not including the weight of the additives in the electrode. The electrode in the discharged state was opened in a dry box, and the material was washed with DEC and dried with cotton. This recovered powder was mixed with liquid paraffin oil, smeared on a glass substrate, and covered by an adhesive tape on the surface to prevent the sample from reacting with oxygen and mixture during the XRD measuring process.[18]

Results and Discussion

Structural Determination. Figure 1 shows the typical XRD patterns of the as-prepared $Ag_2V_4O_{11}$ nanowires, α-$AgVO_3$ microrods, and β-$AgVO_3$ nanowires and their corresponding crystal structures. All the diffraction peaks in Figure 1a can be readily indexed to pure phase of $Ag_2V_4O_{11}$ with the monoclinic structure [space group: *C*2/*m* (No. 12), JCPDS-ICDD Card No.49-0166]. No peaks from other phases have been detected, indicating that the products are of high purity. Rietveld refinement of XRD patterns in Figures 1c and 1e can be well indexed to pure monoclinic phase of α- and β-$AgVO_3$, respectively. It can be seen that the refined patterns fit the observed data points very well. The cell parameters of α-$AgVO_3$ can be determined to be $a = 10.443(2)$ Å, $b = 9.910(2)$ Å, $c = 5.531(1)$ Å, and $\beta = 99.70(2)°$, which are in good agreement with the standard values [space group: *C*2/*c* (No. 15), JCPDS-ICDD Card No. 89-4396]. The refined cell parameters of β-$AgVO_3$ are $a = 18.069(1)$ Å, $b = 3.590(2)$ Å, $c = 8.013(3)$ Å, and $\beta = 104.45(4)°$, which correspond well with the standard values [space group: *Cm* (No. 8), JCPDS-ICDD Card No. 86-1154].

In addition, the observed broadening diffraction peaks for $Ag_2V_4O_{11}$ indicate that the crystalline size of the sample is very fine and that the crystallinity is not as good as that of α- and β-$AgVO_3$. The crystal structure of $Ag_2V_4O_{11}$, as shown in Figure 1b, consists of $[V_4O_{16}]$ units made of VO_6 distorted octahedrons sharing their apexes, which build infinite $[V_4O_{12}]_n$ quadruple strings. These quadruple strings are linked by corner-shared oxygen to provide continuous $[V_4O_{11}]_n$ layers separated by silver atoms. Comparing the structure of β-$AgVO_3$ (Figure 1f) with that of $Ag_2V_4O_{11}$ (Figure 1b), one can see that they are built with the same quadruple $[V_4O_{12}]_n$ chains, which are isolated in β-$AgVO_3$, but corner-shared in $Ag_2V_4O_{11}$. On the other hand,

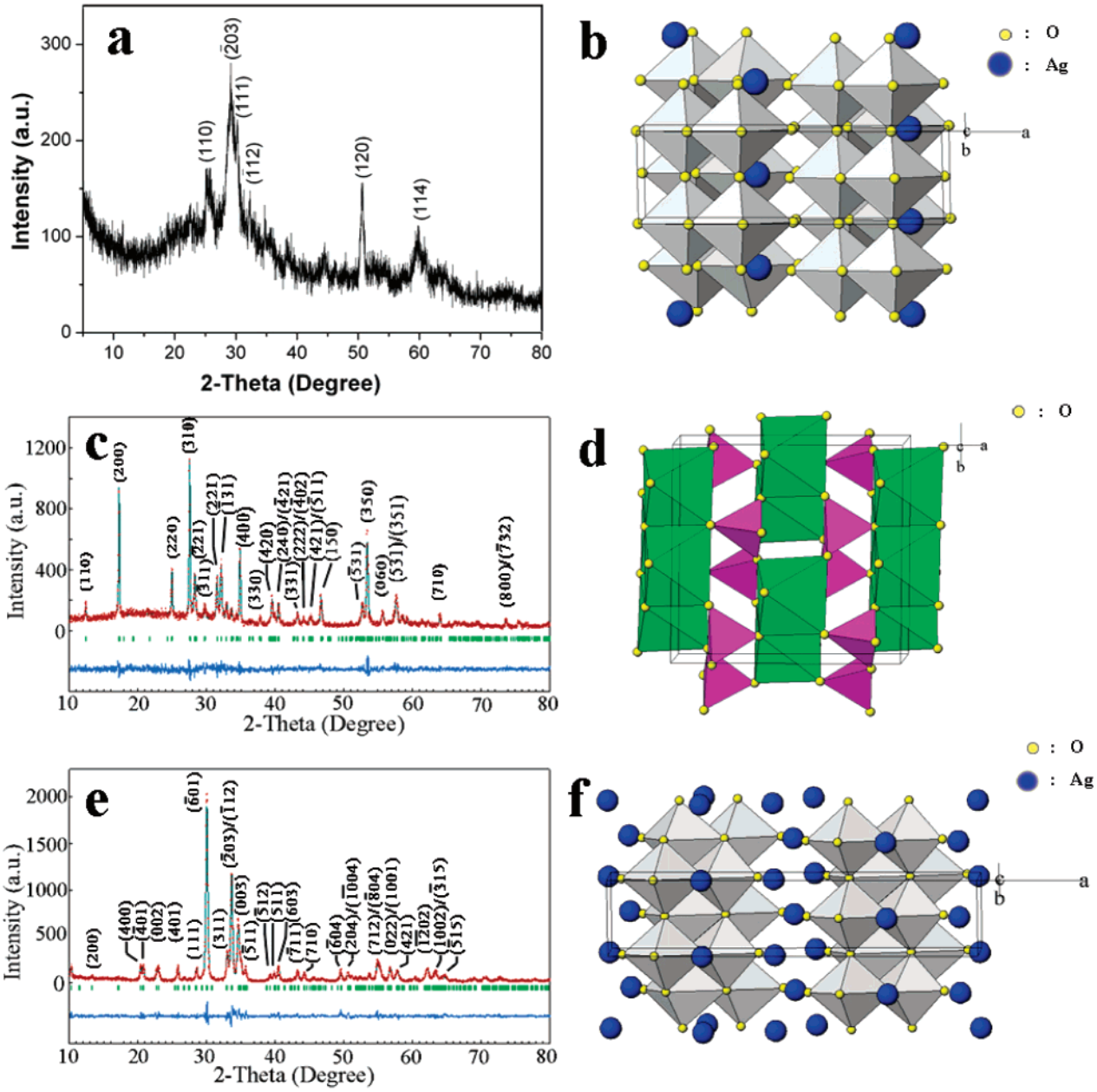

Figure 1. XRD pattern (a) and crystal structure (b) of the as-prepared $Ag_2V_4O_{11}$ nanowires. Rietveld refinement of XRD profile (c) and crystal structure (d) of α-$AgVO_3$ microrods. Rietveld refinement of XRD profile (e) and crystal structure (f) of β-$AgVO_3$ nanowires. Note that in parts c and e the red lines are observed intensities and the blue lines are calculated intensity. Vertical bars below the patterns show the positions of all possible reflection peaks. The bottom solid lines show the difference between the calculated and observed intensities.

the structure of α-$AgVO_3$ is quite different from that of β-$AgVO_3$ and $Ag_2V_4O_{11}$. As in α-$AgVO_3$, the zigzag chains of tetrahedrons of VO_4 are sandwiched between the sheets of Ag-centered octahedrons sharing the edges along c-direction, resulting the smaller atomic packing compared with the V-centered octahedrons in β-$AgVO_3$.

Morphology Characterization. Figures 2a and 2b display the representative SEM images of the as-prepared $Ag_2V_4O_{11}$ nanowires at different magnifications. The relatively low-magnification image (Figure 2a) shows a typical overall view of the $Ag_2V_4O_{11}$ nanowires. It is observed that a large number of nanowires with the lengths of about several tens of micrometers are distributed homogeneously over a wide area, indicating that a significant proportion (about 95%) of the product is present in a long, wirelike morphology. A higher magnification image (Figure 2b) shows that several of the nanowires are arranged roughly parallel to one another and tightly bundled together. The nanowire diameter distribution (see the Supporting Information, Figure S1a) shows that the average diameter of the nanowires is 38.9 ± 2.4 nm. The detailed morphology and microstructure of the $Ag_2V_4O_{11}$ nanowires was further characterized by TEM and HRTEM. The TEM image (Figure 2c) shows that the nanowires are approximately 30−50 nm in diameter, indicating a high aspect ratio of above 1000. Figure 2d is the TEM image of an individual nanowire at higher magnification, which shows that tiny nanoparticles with a diameter of approximately 5−10 nm are attached on the nanowires. The tiny nanoparticles on the $Ag_2V_4O_{11}$ nanowires were analyzed by energy dispersive spectroscopy (EDS), as shown in Figure 1Sd. The C and Cu presence is due to the supporting substrate, and the atomic ratio of Ag:V:O is approximately 2:4:11, confirming the composition of the tiny nanoparticles of $Ag_2V_4O_{11}$. In addition, the XRD patterns also demonstrate the single phase of the product, and no evidence

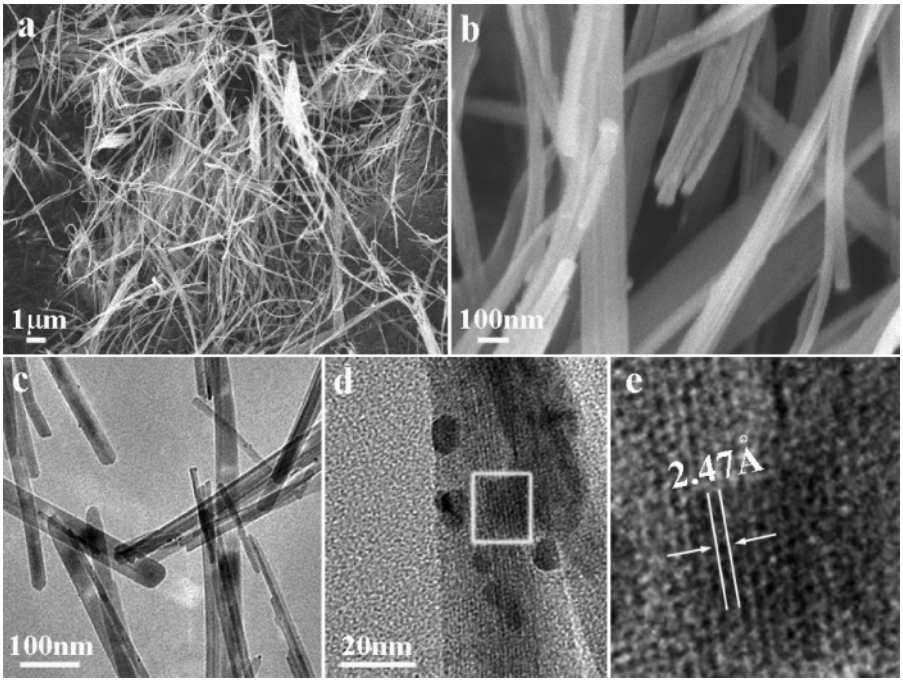

Figure 2. (a, b) SEM and (c, d) TEM images of the as-prepared $Ag_2V_4O_{11}$ nanowires at different magnifications. (e) The corresponding HRTEM image of the area marked in d.

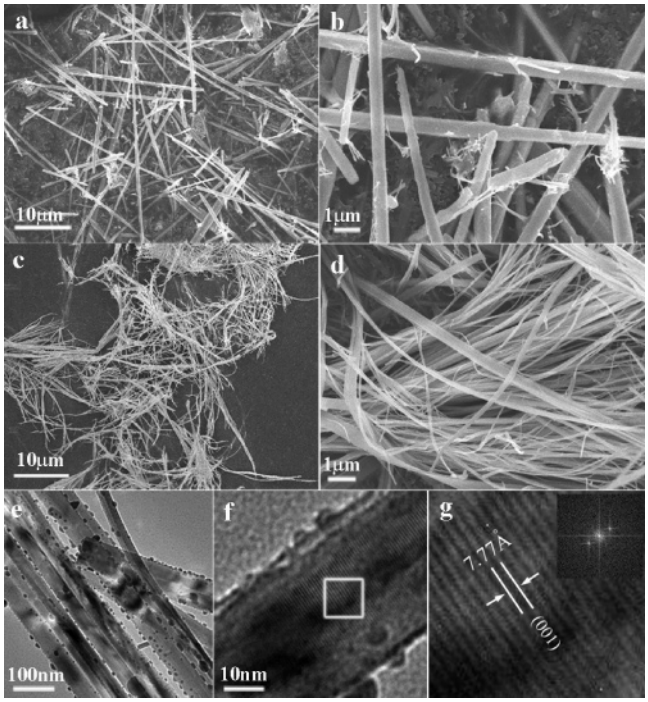

Figure 3. SEM images of the (a, b) α-$AgVO_3$ microrods and (c, d) β-$AgVO_3$ nanowires. (e, f) TEM images of the β-$AgVO_3$ nanowires, and (g) HRTEM image of the area marked in f. The inset of g shows the corresponding FFT pattern.

of impurity compounds were observed. The HRTEM image of the area marked by a white solid square in Figure 2d is shown in Figure 2e. Clear fringes with an interplanar spacing of 0.247 nm, which corresponds to the separation between (−603) lattice planes, are aligned parallel to the longitudinal direction of the nanowire.

Typical SEM images of the as-synthesized α-$AgVO_3$ microrods and β-$AgVO_3$ nanowires are depicted in Figures 3a−d. The diameter of the α-$AgVO_3$ microrods is in the range of 600−900 nm, and the length is about several tens of micrometers (Figures 3a and 3b). The histogram of the microrod diameter distribution displays that the diameter distribution is broad and the mean diameter is 681.8 ± 8.3 nm (Figure S1b). The SEM image in Figure 3c shows that large quantities of β-$AgVO_3$ nanowires with the lengths of several tens of micrometers were obtained, while the SEM image in Figure 3d at a higher magnification shows that the nanowires are around 50 nm in diameter. Although there are a small amount of large fiber bundles with diameter about 1 μm, the histogram of the nanowire diameter distribution (Figure S1c) clearly indicates that the β-$AgVO_3$ nanowires have a relatively centralized diameter distribution, and the average diameter of the nanowires is 46.6±0.5 nm. Furthermore, the morphology of the as-synthesized β-$AgVO_3$ was dramatically influenced by the initial pH of the precursor mixture (Figure S2). The results indicate that the diameter of the 1D β-$AgVO_3$ nano/microstructures can be simply controlled in the range of 40 nm to 1 μm by titrating the pH of the precursor mixture. The TEM images (Figures 3e and 3f) clearly reveal that the diameter of the β-$AgVO_3$ nanowires is in the range of 40−50 nm, which is consistent with the observation in SEM images, and a lot of tiny nanoparticles are attached on the backbone of the β-$AgVO_3$ nanowires. Figure 3g shows the HRTEM image of the area marked by a white solid square in Figure 3f. Clear fringes perpendicular to the longitudinal direction of the nanowire with an interplanar spacing of approximately 0.777 nm were observed, which corresponds to the separation between (001) lattice planes. This was also reflected in the corresponding fast Fourier transform (FFT) pattern (inset, Figure 3 g).

Formation of 1-D $AgVO_3$ Nano/Microstructures. In our experiment, the phase transformation from α-$AgVO_3$ to β-$AgVO_3$ was controlled by the dwell time of the hydrothermal treatment, as monitored by the XRD patterns of the products (Figure S3). α-$AgVO_3$ was obtained during the reaction time of 0−4 h. The diffraction peaks for α-$AgVO_3$ completely vanished when the reaction time was extended to 6 h, which corresponds to the formation of β-$AgVO_3$. The intensity of the peaks for β-$AgVO_3$ gradually increased with further increased

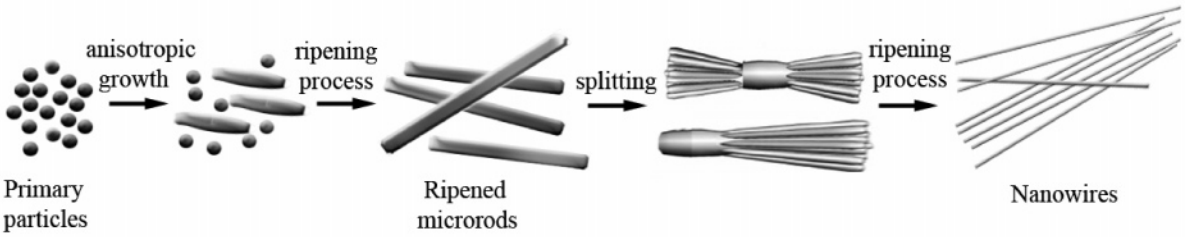

Figure 4. Schematic diagram showing the growth process of 1-D $AgVO_3$ nano/ microstructures.

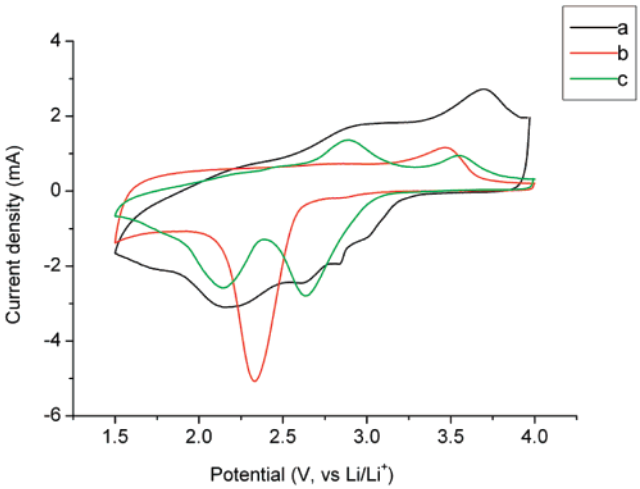

Figure 5. CVs of the electrodes made from the as-prepared (a) $Ag_2V_4O_{11}$ nanowires, (b) α-$AgVO_3$ microrods, and (c) β-$AgVO_3$ nanowires in the first cycle at a scan rate of 1 mV s^{-1} and a temperature of 37 °C.

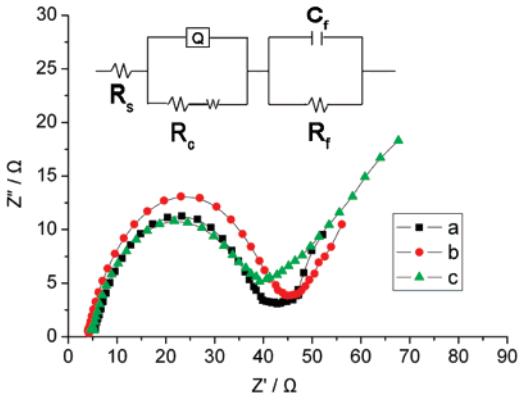

Figure 6. Impedance spectra of the electrodes made from the as-prepared (a) $Ag_2V_4O_{11}$ nanowires, (b) α-$AgVO_3$ microrods, and (c) β-$AgVO_3$ nanowires under the open-circuit condition.

reaction time, and β-$AgVO_3$ with good crystallinity was obtained when the reaction time was prolonged to 15 h. Meanwhile, the morphological evolution of the products took place with increasing hydrothermal reaction time (Figure S4). Based on the present experimental results, a "ripening−splitting model" was proposed to elucidate the formation of 1-D $AgVO_3$ nano/ microstructures, and the whole process can be schematically illustrated in Figure 4. The initial growth mechanism of α-$AgVO_3$ microrods in the solution system is the well-known "Ostwald-ripening process",[19] in which, the formation of tiny crystalline nuclei in a supersaturated medium occurs at first and then is followed by crystal growth. With the reaction going on, the irregular particles vanish and the longer microrods start to form, suggesting that the longer microrods grow at the expense of smaller particulates due to the energy difference between large particles and smaller particles of a higher solubility based on the Gibbs−Thompson Law. Then, "a splitting process" occurs in which the α-$AgVO_3$ microrods split into β-$AgVO_3$ nanowires. As reported, α-$AgVO_3$ is a metastable phase and can be irreversibly transformed into β-$AgVO_3$ at around 200 °C.[20] Under hydrothermal conditions (at 180 °C and relatively high pressure), an α→β phase transformation takes place. Therefore, the microrods structures split into nanowires with the phase transformation, and this is why rice-strawlike structures were observed by SEM (Figures S4c−f).

Electrochemical Properties. Figure 5 shows the cyclic voltammograms (CVs) of the electrodes made from the as-prepared $Ag_2V_4O_{11}$ nanowires, α-$AgVO_3$ microrods, and β-$AgVO_3$ nanowires in the first cycle at a scan rate of 1 mV s^{-1} and a temperature of 37 °C. The shapes of the CV curves of the three representative electrodes are quite different. The $Ag_2V_4O_{11}$ nanowire electrode (Figure 5a), in the cathodic polarization process, four peaks were observed at around 3.02, 2.84, 2.62, and 2.18 V versus Li^+/Li, corresponding to the complicated multistep electrochemical lithium intercalation processes; while in the following anodic polarization, two characteristic peaks were located at 3.68 and 2.92 V, corresponding to the lithium extraction processes. For the α-$AgVO_3$ microrod electrode (Figure 5b), only one strong peak appeared at 2.33 V when the electrode was scanned cathodically, and only one anodic peak can be observed at 3.47 V. Meanwhile, for β-$AgVO_3$ nanowire electrode (Figure 5c), two strong cathodic peaks were located at 2.64 and 2.15 V, and two anodic peaks were seen at 2.89 and 3.55 V, indicating that the lithium insertion/deinsertion mechanism of β-$AgVO_3$ is quite different from that of α-$AgVO_3$.

Figure 6 shows the typical impedance spectra of the electrodes made from the as-prepared $Ag_2V_4O_{11}$ nanowires, α-$AgVO_3$ microrods, and β-$AgVO_3$ nanowires under the open-circuit condition. The impedance spectra of the three electrodes have a similar shape with a depressed semicircle in the high-frequency region and a straight line with an angle of approximately 45° relative to the real axis in the low-frequency region. The semicircle can be interpreted as resulting from the charge-transfer process and the passivating film formed on the SVO. The linear portion is designated to Warburg impedance, indicating the presence of diffusion limitations for lithium inside the SVO. The inset is the equivalent circuit for the impedance spectra. R_s is the combination of electrolyte resistance and ohmic resistances of cell components. R_f and R_c are the film resistance and charge-transfer resistances, respectively. C_f is the capacity corresponding to R_f, and Q_c refers to the constant phase element. There is no difference in the physical meaning between a capacitor and constant phase element, except that a constant phase element is an imperfect capacitor. W is the Warburg impedance. A similar type of equivalent circuit had been used by others for reversibly intercalating cathodes.[21]

Figure 7 displays the initial discharge curves of the electrodes made from the $Ag_2V_4O_{11}$ nanowires, α-$AgVO_3$ microrods, and β-$AgVO_3$ nanowires at a constant current of 0.01 mA to the

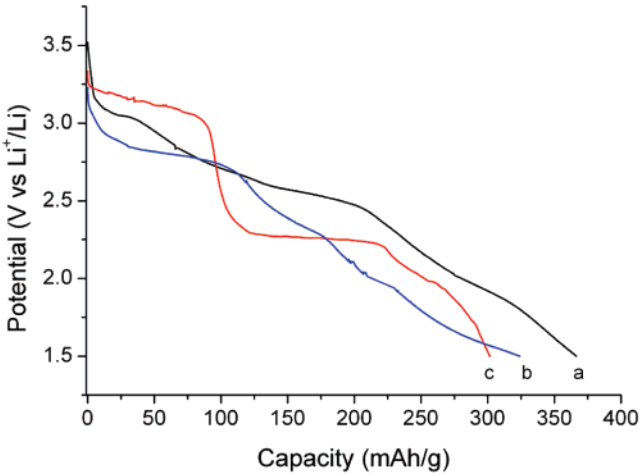

Figure 7. Discharge curves as a function of capacity for the electrodes made from the as-prepared (a) $Ag_2V_4O_{11}$ nanowires, (b) α-$AgVO_3$ microrods, and (c) β-$AgVO_3$ nanowires at a constant current of 0.01 mA and the temperature of 37 °C.

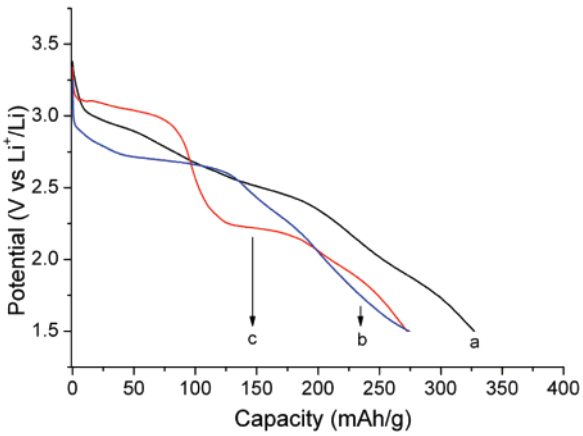

Figure 8. Discharge curves as a function of capacity for the electrodes made from the as-prepared (a) $Ag_2V_4O_{11}$ nanowires, (b) α-$AgVO_3$ microrods, and (c) β-$AgVO_3$ nanowires at a constant current of 0.1 mA and the temperature of 37 °C.

cutoff voltage of 1.5 V and at the temperature of 37 °C. It can be seen that the as-prepared $Ag_2V_4O_{11}$ nanowire electrode (Figure 7a) displays a discharge curve with four sloping potential ranges (3.10−2.95 V, 2.84−2.62 V, 2.60−2.35 V, and 2.15−1.70 V vs Li^+/Li) for the lithium intercalation reaction, in accordance with the four cathodic peaks in the above CV in Figure 5a. The initial open circuit voltage is about 3.52 V, and the discharge capacity is as high as 366 mAh g^{-1}, which is equivalent to an intercalation of approximately 8.1 Li per formula unit (~$Li_{8.1}Ag_2V_4O_{11}$). For comparison purposes, we also evaluated the performance of the $Ag_2V_4O_{11}$ bulk particles obtained from solid-state reaction (Figure S5). It is found that the $Ag_2V_4O_{11}$ bulk powder electrode delivers a much lower discharge capacity of about 319 mAh g^{-1} (~$Li_{7.1}Ag_2V_4O_{11}$), and the initial open circuit voltage is nearly 200 mV lower than that of $Ag_2V_4O_{11}$ nanowire electrode (Figure S6).

With respect to $AgVO_3$ electrodes, the discharge curve of α-$AgVO_3$ microrod electrode (Figure 7b) shows a flat plateau at approximately 2.8 V, while that of β-$AgVO_3$ nanowire electrode (Figure 7c) exhibits two distinct plateaus at about 3.2 and 2.3 V. The one discharge plateau for α-$AgVO_3$ and the two plateaus for β-$AgVO_3$ are in good agreement with the cathodic peaks in the above CVs. The initial discharge capacities of the three types of electrodes are ordered as follows: $Ag_2V_4O_{11}$ nanowires (366 mAh g^{-1}) > α-$AgVO_3$ microrods (324.1 mAh g^{-1}) > β-$AgVO_3$ nanowires (302.1 mAh g^{-1}). Moreover, the as-prepared β-$AgVO_3$ nanowire electrode delivers much higher capacity above 3 V than that of both $Ag_2V_4O_{11}$ bulk powder and nanowire electrodes, owing to an increase in the silver content for silver vanadates.[12]

ICDs work most efficiently above 3 V, and therefore increasing the high-voltage component of the ICD cathode would enhance the performance of the ICD. Some previous studies have shown that the silver vanadate with a greater Ag:V molar ratio would increase the high-voltage component of the electrode; however, the total capacity of silver vanadates with a Ag:V ratio greater than 1:2 tends to be much lower than that of $Ag_2V_4O_{11}$.[12,22] Then the point is how to not only enhance the high-voltage component of the Li/SVO battery but also make the battery deliver a relatively high capacity at the same time. The above galvanostatic discharge curves show that the as-prepared β-$AgVO_3$ nanowire electrode with a higher Ag:V molar ratio (1:1) delivers higher capacity above 3 V than that of both $Ag_2V_4O_{11}$ bulk powder and nanowire electrodes, while the total capacity (302.1 mAh g^{-1}) is only a little lower than the commercial $Ag_2V_4O_{11}$ (315 mAh g^{-1}), and therefore could also be a potential cathode material in primary lithium ion batteries. The significantly improved electrochemical capacity of the β-$AgVO_3$ nanowire electrode may be the result of the 1-D nanostructure. It is also noted that although α- and β-$AgVO_3$ have the same Ag:V molar ratio, α-$AgVO_3$ microrod electrode shows much lower capacity above 3 V than β-$AgVO_3$, which might be due to the difference between the crystal structures of α- and β-$AgVO_3$, as discussed later.

The high-rate discharge capability of the electrodes made from the as-prepared $Ag_2V_4O_{11}$ nanowires, α-$AgVO_3$ microrods, and β-$AgVO_3$ nanowires were investigated at a constant current of 0.1 mA and a temperature of 37 °C. As shown in Figure 8, the capacities for the electrodes of $Ag_2V_4O_{11}$ nanowires, α-$AgVO_3$ microrods, and β-$AgVO_3$ nanowires are 327.2, 274.3, and 272.7 mAh g^{-1}, respectively, corresponding to 89.4, 84.6, and 90.3% of their capacities at 0.01 mA; on the other hand, the $Ag_2V_4O_{11}$ bulk electrode only showed 267.3 mAh g^{-1}, corresponding to 83.8% of its capacity at 0.01 mA (Figure S7). As a result, the sequence of their high-rate discharge ability from best to worst is β-$AgVO_3$ nanowires > $Ag_2V_4O_{11}$ nanowires > α-$AgVO_3$ microrods > $Ag_2V_4O_{11}$ bulk.

In addition, the discharge performances of the electrodes made from β-$AgVO_3$ with different morphologies were further investigated in order to explore the possible influence of their shapes and sizes on the electrochemical properties. Figure 9 shows the comparison of the discharge curves for the electrodes made from the as-synthesized β-$AgVO_3$ nanowires, microrods, and bulk particles (see the SEM image of Figure S8) at different discharge currents and the temperature of 37 °C. At 0.01 mA, the discharge profiles of the three electrodes have a similar shape with two plateaus, and the initial open circuit voltages are around 3.34 V. The initial discharge capacities of the three electrodes are ordered as follows: β-$AgVO_3$ nanowires (302.1 mAh g^{-1}) > β-$AgVO_3$ microrods (281.5 mAh g^{-1}) > β-$AgVO_3$ bulk (271.9 mAh g^{-1}). At a higher discharge current of 0.1 mA, it is noticed that the discharge curve of the nanowire electrode exhibits a higher discharging voltage and a longer plateau than that of the microrod and bulk electrodes, indicating a higher power-output behavior. The discharge capacities for β-$AgVO_3$ nanowire and microrod electrodes were still about 272.7 and 225.5 mAh g^{-1} at 0.1 mA, corresponding to 90.3 and 80.1% of their capacities at 0.01 mA, respectively, while the electrode of the bulk particles only showed 194.5 mAh g^{-1} (about 71.5%

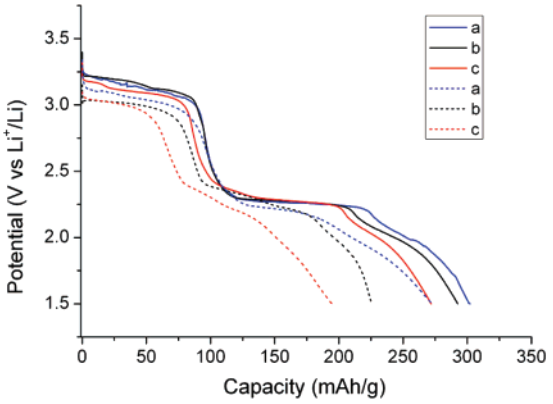

Figure 9. Discharge curves as a function of capacity for the electrodes made from the as-prepared β-$AgVO_3$ (a) nanowires, (b) microrods, and (c) bulk particles at the current density of 0.01 mA and 0.1 mA and the temperature of 37 °C. Solid lines: 0.01 mA. Dotted lines: 0.1 mA.

of its capacity at 0.01 mA). Hence, the high-rate discharge ability from best to worst displays the following order: β-$AgVO_3$ nanowires > β-$AgVO_3$ microrods > β-$AgVO_3$ bulk particles. Therefore, it can be concluded that the discharge capacity and high-rate capability of the electrodes both increase with the decreasing size of the active materials.

According to the results presented above, both $Ag_2V_4O_{11}$ and β-$AgVO_3$ nanowire electrodes exhibit superior electrochemical properties (higher discharge capacity and better high-rate capabilities) to their bulk counterparts. The significantly improved electrochemical properties of the nanowire electrodes may result from the following two factors. One is the fast kinetics related to the unique 1-D nanostructured materials. The diameter of the nanowires is much smaller than the corresponding bulk particles, leading to a higher Li^+ diffusion rate and faster electronic kinetics.[23] The other factor is the relatively high specific surface areas of nanostructured materials. In nanomaterials, an increasing proportion of the total number of the atoms lies near or on the surface, which provides more active sites for the contact between active material and electrolyte and decreases the polarization of the electrode. Furthermore, a lot of tiny nanoparticles attached on the backbone of the nanowires, as shown in Figure 2d and Figure 3e, provide the structural strains to make it more active for the lithium electrochemical reaction.

Electrochemical Reaction Mechanism. Previously, the electrochemical performances of α- and β-$AgVO_3$ have rarely been investigated. Therefore, the electrochemical reaction mechanisms of the α- and β-$AgVO_3$ electrodes are of particular interest. To further understand the reaction mechanism of the electrodes, XPS spectra were taken for the electrodes of α-$AgVO_3$ microrods and β-$AgVO_3$ nanowires during different stages of the discharge process. Figure 10a and 10b show the XPS spectra of the Ag 3d and V 2p for the β-$AgVO_3$ nanowire electrode in the state of discharging to the first plateaus (about 3.0 V) and the second plateaus (about 2.3 V), respectively. As shown in Figure 10a, two peaks located at the binding energy (BE) of 517.1 and 524.5 eV can be attributed to a doublet V^{5+} $2p_{3/2}$ and $2p_{1/2}$, which corresponds well with that of V_2O_5.[24] Meanwhile, peaks for Ag 3d were also observed in Figure 10a, and both the peaks for Ag $3d_{5/2}$ and Ag $3d_{3/2}$ can be deconvoluted into two components, indicating the presence of different valences of silver species. The two strong peaks at the Ag region of 368.4 and 374.4 eV correspond to Ag^0 $3d_{5/2}$ and $3d_{3/2}$, respectively, while the two relatively weak peaks appearing at 367.4 and 373.3 eV can be assigned to Ag^+ $3d_{5/2}$ and $3d_{3/2}$,

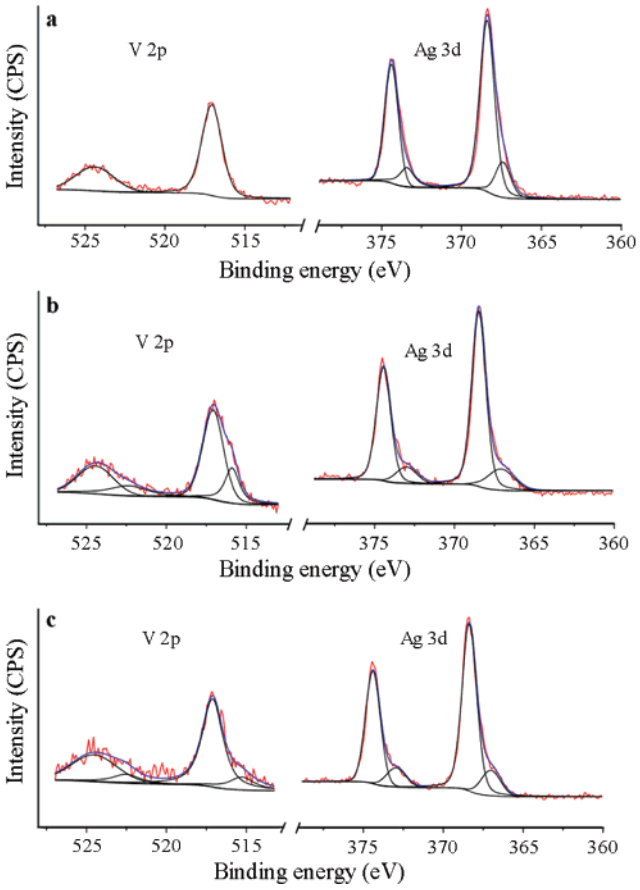

Figure 10. XPS spectra of Ag 3d and V 2p for the electrodes of β-$AgVO_3$ nanowires and α-$AgVO_3$ microrods at different stages of the discharge process: β-$AgVO_3$ nanowires discharged to (a) 3.0 V and (b) 2.3 V. (c) α-$AgVO_3$ microrods discharged to 2.8 V.

indicating that most of Ag^+ was reduced to metallic Ag during the first step of discharge.[25]

When the β-$AgVO_3$ nanowire electrode deeply discharged to the second plateaus of around 2.3 V, a new vanadium state appears with a doublet peaks at the binding energy of 515.8 and 522.4 eV (Figure 10b), revealing the formation of V^{4+} during the electrochemical reaction. Moreover, the characteristic peaks of Ag^+ 3d can still be observed, indicating the existence of the simultaneous reduction from Ag^+ to Ag. The XPS spectra of Ag 3d and V 2p for the α-$AgVO_3$ microrod electrode in the state of discharging to the plateau of 2.8 V are presented in Figure 10c. In contrast to the XPS spectra of β-$AgVO_3$ nanowire electrode in the first discharge plateau (Figure 10a), both Ag 3d and V 2p peaks of α-$AgVO_3$ microrod electrode contain shoulders that are distinguishable in the spectrum, suggesting that the reductions from Ag^+ to Ag^0 and V^{5+} to V^{4+} in α-$AgVO_3$ microrod electrode were not separated like those in β-$AgVO_3$ nanowire electrode, but rather occurred at the same time. The formation of silver in the discharge process was further confirmed by the XRD measurement (Figures S9, 10).

On the basis of the results described above, we propose that lithium ions are intercalated into β-$AgVO_3$ nanowires via two steps that are distinguished by discharge plateau voltages. In the first step, Ag^+ between the vanadium oxide octahedrons layers are reduced to Ag^0 and deposited as metallic silver, and the inserted lithium ions occupy the available sites between the layers. When the discharge process proceeds to the second step, the electrochemical activity shifts from silver to vanadium reduction. The dominant reduction during the second range is from V^{5+} to V^{4+}, as well as partial reduction from V^{4+} to V^{3+}

and Ag^+ to Ag. The two steps of different electrochemical reactions correspond to the two cathodic peaks observed in the CV curve of Figure 5c. The first cathodic peak that corresponds to the first plateau in the discharge profile is assigned to the reduction of Ag^+, and the second cathodic peak corresponding to the second plateau is mainly attributed to the reduction of V^{5+}. In contrast, the electrochemical reaction took place in the α-$AgVO_3$ microrod electrode during discharge is remarkably different from that of β-$AgVO_3$ nanowire electrode. Insertion of lithium into α-$AgVO_3$ microrod results in the simultaneous reduction of the silver and vanadium, and this is consistent with the observation of CV curve for α-$AgVO_3$ microrod electrode (Figure 5b), in which the one strong cathodic peak may be the overlap of the silver and vanadium reduction peaks.

The different electrochemical behaviors of α- and β-$AgVO_3$ electrodes can be attributed to the remarkable differences between the crystal structures of the two electrode materials. As for β-$AgVO_3$, silver ions lie between the sheets of vanadium oxide octahedrons, while vanadium ions occupy the center sites of the vanadium oxide octahedrons, as shown in Figure 1f. The silver interlayer between the vanadium oxide sheets allows for more facile lithium diffusion than the octahedral coordination of the vanadium. Therefore, silver ions were reduced at a higher reduction voltage, while vanadium ions were reduced at a lower reduction voltage. With respect to α-$AgVO_3$, the crystal framework consists of silver oxide octahedron layers and vanadium oxide tetrahedron layers (Figure 1d). The octahedral coordination of silver in α-$AgVO_3$ makes electrochemical reduction of silver ions much more difficult than the silver interlayers in β-$AgVO_3$. Consequently, the presence of vanadium oxide tetrahedrons and silver oxide octahedrons within the crystal framework depresses the reduction potential, thus decreasing the high-voltage component of α-$AgVO_3$ electrode.

According to the results presented above, the Li−SVO batteries made from the $Ag_2V_4O_{11}$ and $AgVO_3$ 1-D nano/microstructures display higher energy density than other cathode materials used in lithium ion batteries (see Supporting Information).[4a,5f] Therefore, the electrochemical properties of the $Ag_2V_4O_{11}$ and $AgVO_3$ 1-D nano/microstructures as cathode materials for rechargeable lithium ion batteries are of particular interest. As an extension of the work on the primary Li−SVO batteries, the electrochemical properties of the β-$AgVO_3$ and $Ag_2V_4O_{11}$ nanowires as the cathode material in rechargeable batteries were also investigated. The result found that the reversibility of β-$AgVO_3$ and $Ag_2V_4O_{11}$ nanowires in Li−SVO cells was undesirable; after 20 charge−discharge cycles, the β-$AgVO_3$ and $Ag_2V_4O_{11}$ nanowires electrodes maintain about 30% and 35% of their initial capacities, respectively. This result is similar to the earlier report, in which the $Ag_2V_4O_{11}$ was found to show a fast capacity decline.[26] The poor reversibility of β-$AgVO_3$ and $Ag_2V_4O_{11}$ probably influenced by volume changes associated with the formation/annihilation of silver particles during the charge/discharge process. However, Kawakita et al. reported that substituting some silver with sodium in $Ag_2V_4O_{11}$ can result in better reversibility, in which sodium ions connect adjacent layers in the material and stabilize the structure.[27] Thus, by modifying or combining it with other components, the as-prepared β-$AgVO_3$ and $Ag_2V_4O_{11}$ 1-D nanostructures are likewise possible to find application as electrode materials in rechargeable batteries.

Conclusions

$Ag_2V_4O_{11}$ nanowires, α-$AgVO_3$ microrods, and β-$AgVO_3$ nanowires have been successfully prepared via a simple and facile low-temperature hydrothermal approach, in which the reaction conditions such as pH and growth time have a determining effect on the structures and morphologies of the Ag−V−O product. Electrochemical measurements of primary lithium ion batteries showed that the electrodes with the as-prepared $Ag_2V_4O_{11}$ nanowires, α-$AgVO_3$ microrods, and β-$AgVO_3$ nanowires exhibited high discharge capacities of 366 mAh g^{-1}, 324.1 mAh g^{-1}, and 302.1 mAh g^{-1}, respectively. Furthermore, those electrodes demonstrate excellent high-rate dischargeability and are promising cathode candidates in the field of primary Li−SVO batteries for ICDs. In particular, the electrode with β-$AgVO_3$ nanowires showed much higher capacity above 3 V than that of α-$AgVO_3$ and $Ag_2V_4O_{11}$. The difference between the α- and β-$AgVO_3$ crystal structures has a predominant influence on the lithium intercalation and electrochemical performance. The high voltage component of the Li−SVO battery with $Ag_2V_4O_{11}$ and $AgVO_3$ 1-D nano/microstructures should contribute to rapidly charging the capacitors in ICDs, which deliver the defibrillating shock to the heart with minimal voltage delay. Furthermore, the $Ag_2V_4O_{11}$ and $AgVO_3$ 1-D nano/microstructures may also find potential applications in rechargeable batteries.

Acknowledgment. This work was supported by the National Distinguished Young Scientific Foundation (20325102) and the National Key-Basic Research Program (2005CB623607). The authors are pleased to thank the encouragement of Professor K. R. Poeppelmeier and partial structural analysis of Professor Q.A. Zhang.

Supporting Information Available: The statistic histogram of the as-prepared 1-D nano/microstructure diameters distribution; SEM images and the diameters distribution of β-$AgVO_3$ microrods obtained at different pH value; XRD patterns of $AgVO_3$ obtained at different hydrothermal dwell time; SEM images of $AgVO_3$ obtained at different hydrothermal dwell time; SEM images of $Ag_2V_4O_{11}$ bulk particles obtained from solid-state reaction at different magnification; discharge curves as a function of capacity for the electrodes made from the as-prepared $Ag_2V_4O_{11}$ bulk particles at the current density of 0.01 mA at 37 °C; discharge curves as a function of capacity for the electrodes made from the as-prepared $Ag_2V_4O_{11}$ bulk particles at the current density of 0.1 mA at 37 °C; SEM images of β-$AgVO_3$ bulk particles obtained from solid-state reaction at different magnification; XRD patterns of α-$AgVO_3$ microrod and β-$AgVO_3$ nanowire electrodes after discharging to the cutoff voltage of 1.5 V; XRD pattern of the PTFE used in the fabrication of the electrodes; comparison of the cathode materials used in rechargeable lithium ion batteries. This material is available free of charge via the Internet at http://pubs.acs.org.

References and Notes

(1) (a) Sun, Y. G.; Xia, Y. N. *Science* **2002**, *298*, 2176. (b) Huang, M. H.; Mao, S.; Feick, H.; Yan, H. Q.; Wu, Y. Y.; Kind, H.; Weber, E.; Russo, R.; Yang, P. D. *Science* **2001**, *292*, 1897.

(2) (a) Hao, E.; Bailey, R. C.; Schatz, G. C.; Hupp, J. T.; Li, S. Y. *Nano Lett.* **2004**, *4*, 327. (b) Kuo, C. L.; Kuo, T. J.; Huang, M. H. *J. Phys. Chem. B* **2005**, *109*, 20115. (c) Magrez, A.; Vasco, E.; Seo, J. W.; Dieker, C.; Setter, N.; Forró, L. *J. Phys. Chem. B* **2006**, *110*, 58.

(3) (a) Zheng, N.; Fan, J.; Stucky, G. D. *J. Am. Chem. Soc.* **2006**, *128*, 6550. (b) Song, R. Q.; Xu, A. W.; Deng, B.; Fang, Y. P. *J. Phys. Chem. B* **2005**, *109*, 22758. (c) Xu, J. S.; Xue, D. F. *J. Phys. Chem. B* **2005**, *109*, 17157.

(4) (a) Bard, A. J.; Faulkner, L. R. *Electrochemical Methods: Fundamentals and Applications*, 2nd ed.; Wiley: Weiheim, Germany, 2001. (b) Linden, D.; Reddy, T. B. *Handbook of Batteries*, 3rd ed.; McGraw-Hill: New York, 2002. (c) Winter, M.; Brodd, R. J. *Chem. Rev.* **2004**, *104*,

4245. (d) Long, J. W.; Dunn, B.; Rolison, D. R.; White, H. S. *Chem. Rev.* **2004**, *104*, 4463.

(5) (a) Kang, K. S.; Meng, Y. S.; Breger, J.; Grey, C. P.; Ceder, G. *Science* **2006**, *311*, 977. (b) Li, G. C.; Pang, S. P.; Jiang, L.; Guo, Z. Y.; Zhang, Z. K. *J. Phys. Chem. B* **2006**, *110*, 9383. (c) Subramanian, V.; Zhu, H. W.; Wei, B. Q. *J. Phys. Chem. B* **2006**, *110*, 7178. (d) Tarascon, J. M.; Armand, M. *Nature* **2001**, *414*, 359. (e) Li, X. X.; Cheng, F. Y.; Guo, B.; Chen, J. *J. Phys. Chem. B* **2005**, *109*, 14017. (f) Tarascon, J. M.; Armand, M. *Nature* **2001**, *414*, 359.

(6) Whittingham, M. S. *Chem. Rev.* **2004**, *104*, 4271.

(7) Takeuchi, K. J.; Marschilok, A. C.; Davis, S. M.; Leising, R. A.; Takeuchi, E. S. *Coord. Chem. Rev.* **2001**, *219*−221, 283.

(8) (a) Skarstad, P. M. *J. Power Sources* **2004**, *136*, 263. (b) Crespi, A.; Schmidt, C.; Norton, J.; Chen, K. M.; Skarstad, P. *J. Electrochem. Soc.* **2001**, *148*, A30. (c) Leising, R. A.; Takeuchi, E. S. *Chem. Mater.* **1994**, *6*, 489.

(9) (a) Crespi, A. M. U.S. Patent 5,221,453, Jun 22, 1993. (b) Liang, C. C.; Bolster, M. E.; Murphy, R. M. U. S. Patent 4,310,609, Jan 12, 1982.

(10) Mao, C. J.; Wu, X. C.; Pan, H. C.; Zhu, J. J.; Chen, H. Y. *Nanotechnology* **2005**, *16*, 2892.

(11) Shen, G. Z.; Chen, D. *J. Am. Chem. Soc.* **2006**, *128*, 11762.

(12) Sorensen, E. M.; Izumi, H. K.; Vaughey, J. T.; Stern, C. L.; Poeppelmeier, K. R. *J. Am. Chem. Soc.* **2005**, *127*, 6347.

(13) Liu, Y.; Zhang, Y. G.; Hu, Y. H.; Qian, Y. T. *Chem. Lett.* **2005**, *34*, 146.

(14) Sharma, S.; Panthöfer, M.; Jansen, M.; Ramanan, A. *Mater. Chem. Phys.* **2005**, *91*, 257.

(15) Xie, J. G.; Cao, X. Y.; Li, J. X.; Zhan, H.; Xia, Y. Y.; Zhou, Y. H. *Ultrason. Sonochem.* **2005**, *12*, 289.

(16) Liu, S. W.; Wang, W. Z.; Zhou, L.; Zhang, L. S. *J. Cryst. Growth* **2006**, *293*, 404.

(17) (a) Gou, X. L.; Cheng, F. Y.; Shi, Y. H.; Zhang, L.; Peng, S. J.; Chen, J.; Shen, P. W. *J. Am. Chem. Soc.* **2005**, *128*, 7222. (b) Cai, F. S.; Zhang, G. Y.; Chen, J.; Gou, X. L.; Liu, H. K.; Dou, S. X. *Angew. Chem., Int. Ed.* **2004**, *43*, 4212. (c) Chen, J.; Li, S. L.; Tao, Z. L.; Shen, Y. T.; Cui, C. X. *J. Am. Chem. Soc.* **2003**, *125*, 5284.

(18) (a) Chen, J.; Xu, L. N.; Li, W. Y.; Gou, X. L. *Adv. Mater.* **2005**, *17*, 582. (b) Li, W. Y.; Xu, L. N.; Chen, J. *Adv. Funct. Mater.* **2005**, *15*, 851. (c) Chen, J.; Kuriyama, N.; Xu, Q.; Takeshita, H. T.; Sakai, T. *J. Phys. Chem. B* **2001**, *105*, 11214. (d) Li, W. Y.; Cheng, F. Y.; Tao, Z. L.; Chen, J. *J. Phys. Chem. B* **2006**, *110*, 119.

(19) (a) Tang, Z. Y.; Wang, Y.; Shanbhag, S.; Giersig, M.; Kotov, N. A. *J. Am. Chem. Soc.* **2006**, *128*, 6730. (b) Li, R. F.; Luo, Z. T.; Papadimitrakopoulos, F. *J. Am. Chem. Soc.* **2006**, *128*, 6280. (c) Peng, Z. A.; Peng, X. G. *J. Am. Chem. Soc.* **2001**, *123*, 1389.

(20) Kittaka, S.; Matsuno, K.; Akashi, H. *J. Solid State Chem.* **1999**, *142*, 360.

(21) Takami, N.; Satoh, A.; Hara, M.; Ohsaki, T. *J. Electrochem. Soc.* **1995**, *142*, 371.

(22) Takeuchi, E. S.; Piliero, P. *J. Power Sources* **1987**, *21*, 133.

(23) (a) Ogasawara, T.; Debart, A.; Holzapfel, M.; Novak, P.; Bruce, P. G. *J. Am. Chem. Soc.* **2006**, *128*, 1390. (b) Cheng, F. Y.; Chen, J.; Gou, X. L.; Shen, P. W. *Adv. Mater.* **2005**, *17*, 2753.

(24) Chenakin, S. P.; Silvy, R. P.; Kruse, N. *J. Phys. Chem. B* **2005**, *109*, 14611.

(25) (a) Weaver, J. F.; Hoflund, G. B. *Chem. Mater.* **1994**, *6*, 1693. (b) Gaarenstroom, S. W.; Winograd, N. *J. Chem. Phys.* **1977**, *67*, 3500.

(26) West, K.; Crespi, A. M. *J. Power Sources* **1995**, *54*, 334.

(27) Kawakita, J.; Makino, K.; Katayama, Y.; Miura, T.; Kishi, T. *J. Power Sources* **1998**, *75*, 244.